The Astronomical Journal, 137:4824–4833, 2009 June doi:10.1088/0004-6256/137/6/4824
© 2009. The American Astronomical Society. All rights reserved. Printed in the U.S.A.

# THE DISCOVERY OF A MASSIVE CLUSTER OF RED SUPERGIANTS WITH GLIMPSE

Michael J. Alexander[1], Henry A. Kobulnicky[1], Dan P. Clemens[2], Katherine Jameson[2], April Pinnick[2], and Michael Pavel[2]
[1] Department of Physics and Astronomy, University of Wyoming, Laramie, WY 82071, USA
[2] Institute for Astrophysical Research, 725 Commonwealth Avenue, Boston University, Boston, MA 02215, USA
*Received 2008 November 6; accepted 2009 March 12; published 2009 April 29*

## ABSTRACT

We report the discovery of a previously unknown massive Galactic star cluster at $\ell = 29\overset{\circ}{.}22$, $b = -0\overset{\circ}{.}20$. Identified visually in mid-IR images from the *Spitzer* GLIMPSE survey, the cluster contains at least eight late-type supergiants, based on follow-up near-IR spectroscopy, and an additional 3–6 candidate supergiant members having IR photometry consistent with a similar distance and reddening. The cluster lies at a local minimum in the $^{13}$CO column density and 8 $\mu$m emission. We interpret this feature as a hole carved by the energetic winds of the evolving massive stars. The $^{13}$CO hole seen in molecular maps at $V_{\rm LSR} \sim 95$ km s$^{-1}$ corresponds to near/far kinematic distances of 6.1/8.7 $\pm$ 1 kpc. We calculate a mean spectrophotometric distance of $7.0^{+3.7}_{-2.4}$ kpc, broadly consistent with the kinematic distances inferred. This location places it near the northern end of the Galactic bar. For the mean extinction of $A_V = 12.6 \pm 0.5$ mag ($A_K = 1.5 \pm 0.1$ mag), the color–magnitude diagram of probable cluster members is well fit by isochrones in the age range 18–24 Myr. The estimated cluster mass is ~20,000 $M_\odot$. With the most massive original cluster stars likely deceased, no strong radio emission is detected in this vicinity. As such, this red supergiant (RSG) cluster is representative of adolescent massive Galactic clusters that lie hidden behind many magnitudes of dust obscuration. This cluster joins two similar RSG clusters as residents of the volatile region where the end of our Galaxy's bar joins the base of the Scutum-Crux spiral arm, suggesting a recent episode of widespread massive star formation there.

*Key words:* Galaxy: stellar content – infrared: stars – open clusters and associations: general

## 1. INTRODUCTION

The *Spitzer Space Telescope* (*SST*) and the Galactic Legacy Infrared Mid-Plane Survey Extraordinaire (GLIMPSE; Benjamin et al. 2003) have opened new windows into many aspects of star formation and Galactic structure. The GLIMPSE mid-IR survey and many complementary surveys such as MIPSGAL (Carey et al. 2005) at 24 $\mu$m, Two Micron All Sky Survey (2MASS; Skrutskie et al. 2006), and the Boston University Five College Radio Astronomy Observatory (BU-FCRAO) Galactic Ring Survey (GRS) in $^{13}$CO (Jackson et al. 2006) together constitute powerful new probes at 1–30 arcsec resolutions of previously obscured components of the Milky Way. These overlapping surveys have produced many new discoveries including a new globular cluster (Kobulnicky et al. 2005) and new young open clusters (Mercer et al. 2005; Figer et al. 2006; Davies et al. 2007). A more complete census of star clusters enables a better understanding of the Galaxy's formation and structure, its star formation history, and its current rate of star formation.

Massive stars are rare and short-lived. A typical 9 $M_\odot$ star will spend about 26 Myr on the main sequence (MS), while a 15 $M_\odot$ star has a MS lifetime of around 13 Myr (Meynet & Maeder 2000). After leaving the MS these stars begin their helium burning red supergiant (RSG) phase. The He-burning lifetime is about 4 Myr for 9 $M_\odot$, 2.5 Myr for 15 $M_\odot$, and even shorter for higher mass stars (Meynet & Maeder 2000). This is a very small window for observing these evolved stars and the reason why there are relatively few of them known in the Galaxy. Bertelli et al. (1994) discovered five RSGs in NGC 7419, and more recently Figer et al. (2006) discovered 14 RSGs and a yellow (G-type) supergiant in single Galactic cluster. The current record holder for the most number of RSGs in a single Galactic cluster is Stephenson 2, also known as RSGC2 (Stephenson 1990; Davies et al. 2007), which has 26 cluster RSGs. The number of massive RSGs in a cluster places strong limits on cluster age (massive stars have not all disappeared yet), cluster mass (enough initial mass to produce large numbers of high-mass stars), and the duration of the star formation burst that produced the cluster, in that the stars must have formed in a relatively short period to have reached the same evolved state simultaneously. Figer et al. (2006) and Davies et al. (2007) use an evolved initial mass function (IMF) to derive initial cluster masses of 20,000–40,000 $M_\odot$ for RSGC1 and RSGC2.

In this paper, we describe the discovery of another RSG cluster using methods similar to those of Figer et al. (2006). The cluster was discovered serendipitously as a conspicuous grouping of bright red stars while perusing three-band mid-infrared (mid-IR) color mosaics from GLIMPSE. At $\ell = 29\overset{\circ}{.}223$ and $b = -0\overset{\circ}{.}207$, the cluster lies in roughly the same direction as the RSG clusters reported in Figer et al. (2006) and Davies et al. (2007). We use archive data from *Spitzer*, 2MASS, and the GRS, along with new near-IR spectroscopy of nine probable members to constrain the stellar content, age, and distance of this young and massive Galactic cluster.

## 2. DATA SETS EMPLOYED

### 2.1. Infrared Archival Data

Our discovery and analysis make use of archival data from the *SST* GLIMPSE I/II and MIPSGAL I legacy surveys. The GLIMPSE (Benjamin et al. 2003) project was conducted using the Infrared Array Camera (IRAC; Fazio et al. 2004) wavebands centered near 3.6, 4.5, 5.8, and 8.0 $\mu$m.[3] With 4 s of integration time per target, 5$\sigma$ sensitivities of 0.2, 0.2, 0.4, and 0.4 mJy

[3] GLIMPSE and MIPSGAL data are available from the *Spitzer* Science Center Web site http://ssc.spitzer.caltech.edu/

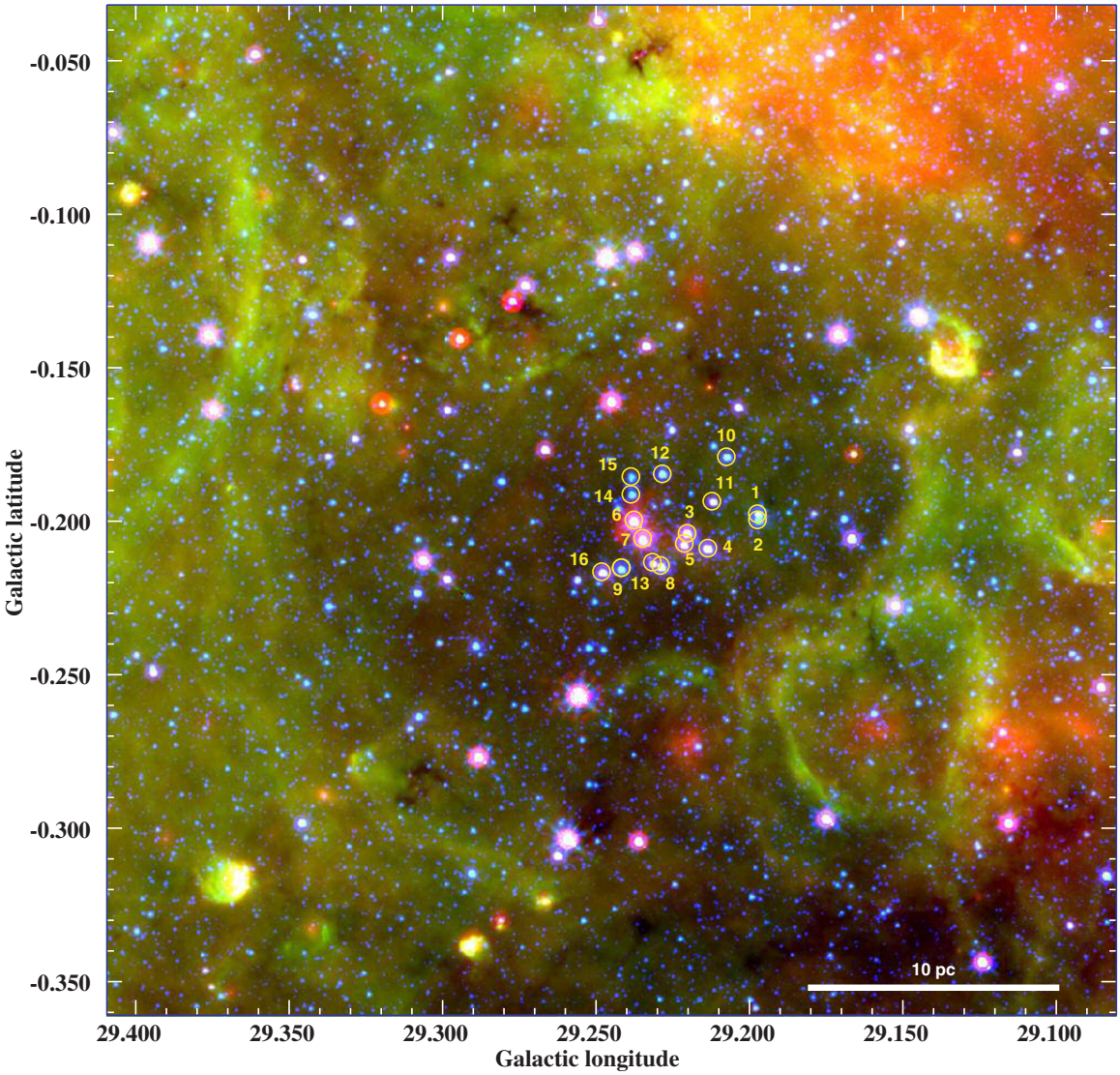


**Figure 1.** Three-color IRAC and MIPS image of the cluster region with 4.5 $\mu$m in blue, 8.0 $\mu$m in green, and 24 $\mu$m in red. Numbered circles 1–9 denote cluster stars with follow-up near-IR spectroscopy, while 10–16 are candidate cluster0 stars near the cluster core. The bar at lower right shows a linear scale of 10 pc at the adopted cluster distance of 7.0 kpc.

were achieved for each band, respectively, on point sources with angular resolutions of $\sim 2''$. In total, the GLIMPSE I implementation covers $|\ell| = 10°$–$65°$ and $|b| < 1°$. Each image was calibrated by the *Spitzer Science Center* and further processed by the GLIMPSE team pipeline to produce point-source catalogs (PSCs) and $3° \times 2°$ mosaics. The *SST* MIPSGAL survey (Carey et al. 2005) covers the same region of sky as GLIMPSE but uses the Multiband Infrared Photometer for Spitzer (MIPS; Rieke et al. 2004) bandpasses at 24, 70, and 160 $\mu$m. The 24 $\mu$m mosaics have a resolution of $6''$ and a $5\sigma$ sensitivity of 1.7 mJy (Carey et al. 2005).

Figure 1 shows a three-color image of the star cluster field, with *Spitzer* IRAC [4.5] in blue, IRAC [8.0] in green, and MIPS [24] in red. Blue predominantly highlights the stellar photospheres. Green shows diffuse emission from warm molecular cloud interfaces, i.e., polycyclic aromatic hydrocarbon (PAH) emission from photodissociation regions excited by UV photons. Red preferentially reveals warm dust. The scale bar in the lower right shows a linear scale of 10 pc at a distance of 7.0 kpc. The grouping of bright stars near the center of the image suggests a physical association. They also lie near a local minimum in the diffuse emission, possibly a cavity sculpted by the winds and energetic photons from young massive stars. Infrared dark clouds (IRDCs) and dark filaments appear superimposed on the bright diffuse background at many locations across this field, indicating the presence of opaque, cold clouds in the foreground. A handful of very red and bright sources, often coinciding with dark clouds, surround the cluster. The color and placement of these objects suggest that they are young stellar objects (YSOs) associated with the IR emission.

We also use photometry from the University of Massachusetts 2MASS (Skrutskie et al. 2006), which observed the sky in the near-IR for $J$ (1.25 $\mu$m), $H$ (1.65 $\mu$m), and $K_s$ (2.16 $\mu$m) bands. The project attained magnitude limits of $J = 15.9$, $H = 15.0$, and $K_s = 14.3$, with a signal-to-noise ratio of 10.

Figure 2 shows a color composite image of the cluster with the 2MASS $J$ band in blue, the $H$ band in green, and the $K_s$ band in red. The brightest cluster stars are conspicuous as a grouping of yellow-red stars near the center of the image.

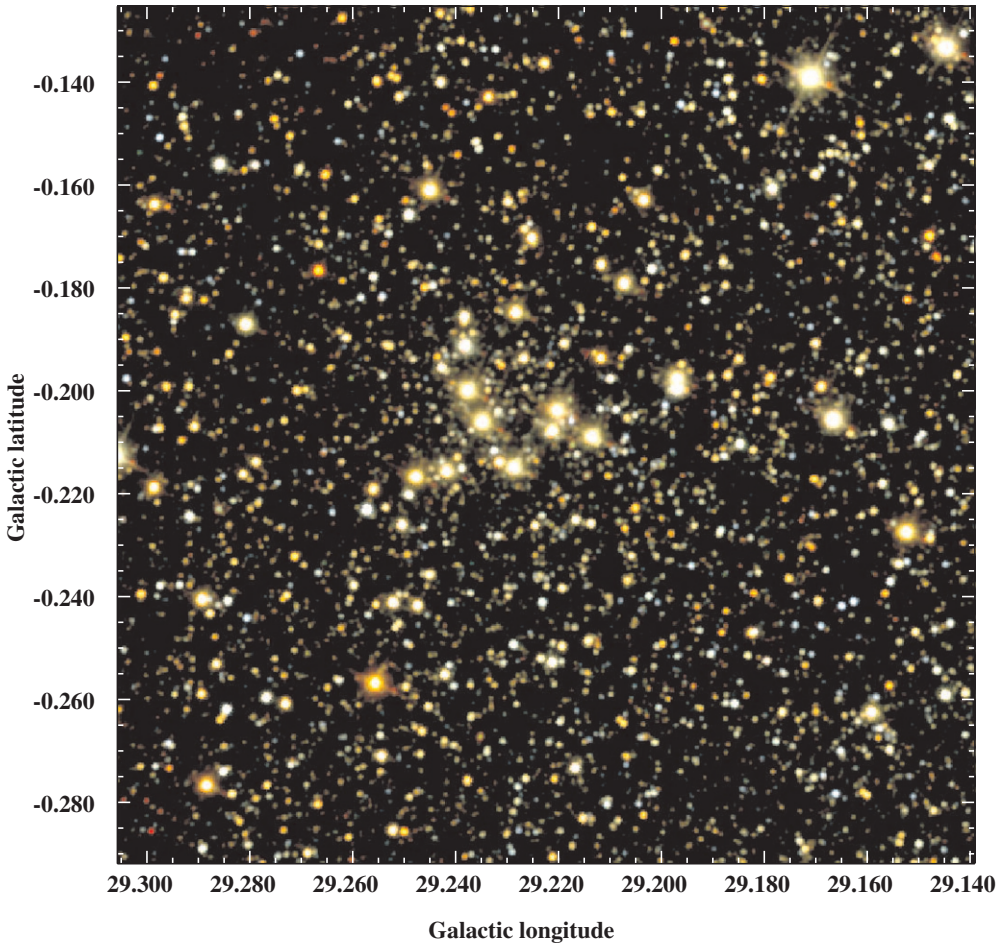


**Figure 2.** Enlarged three-color image of the cluster field with 2MASS *J* band in blue, *H* band in green, and $K_s$ band in red.

**Table 1**
Cluster Members and Candidates

| Star No. | Status[a] | GLIMPSE ID | R.A.(J2000) | Decl.(J2000) | *J* | *H* | $K_s$ | [3.6][b] | [4.5][b] | [5.8] | [8.0] | S.T. |
|---|---|---|---|---|---|---|---|---|---|---|---|---|
| 1 | M | G029.1974 − 00.1975 | 18:45:19.38 | −03:24:48.1 | 9.06 | 6.97 | 6.04 | ... | ... | 5.24 | 5.20 | K5 I |
| 2 | F | G029.1973 − 00.1995 | 18:45:19.81 | −03:24:51.6 | 8.37 | 7.13 | 6.50 | ... | ... | 5.70 | 5.75 | A0 I |
| 3 | M | G029.2206 − 00.2037 | 18:45:23.26 | −03:23:44.0 | 8.51 | 6.52 | 5.51 | ... | ... | 4.45 | 4.20 | M1 I |
| 4 | M | G029.2139 − 00.2087 | 18:45:23.59 | −03:24:13.8 | 8.55 | 6.54 | 5.58 | ... | ... | 4.73 | 4.50 | M0 I |
| 5 | M | G029.2215 − 00.2075 | 18:45:24.17 | −03:23:47.2 | 9.12 | 7.10 | 6.20 | ... | ... | 5.22 | 4.84 | K4 I |
| 6 | M | G029.2380 − 00.1999 | 18:45:24.34 | −03:22:42.0 | 8.54 | 6.43 | 5.35 | ... | ... | 4.19 | 4.14 | M3 I |
| 7 | M | G029.2351 − 00.2059 | 18:45:25.31 | −03:23:01.0 | 8.42 | 6.34 | 5.31 | ... | ... | 4.08 | 4.04 | M2 I |
| 8 | M | G029.2290 − 00.2147 | 18:45:26.52 | −03:23:35.2 | 8.53 | 6.62 | 5.75 | ... | ... | 4.92 | 4.63 | K5 I |
| 9 | M | G029.2421 − 00.2154 | 18:45:28.12 | −03:22:54.5 | 9.34 | 7.26 | 6.29 | ... | ... | 5.49 | 5.44 | K4 I |
| 10 | C | G029.2076 − 00.1790 | 18:45:16.55 | −03:23:44.6 | 9.65 | 7.43 | 6.43 | ... | ... | 5.57 | 5.52 | ... |
| 11 | C | G029.2121 − 00.1935 | 18:45:20.13 | −03:23:54.1 | 11.69 | 8.80 | 7.39 | ... | ... | 5.71 | 5.54 | ... |
| 12 | C | G029.2286 − 00.1846 | 18:45:20.03 | −03:22:46.8 | 9.53 | 7.29 | 6.30 | ... | ... | 5.46 | 5.43 | ... |
| 13 | C | G029.2317 − 00.2137 | 18:45:26.60 | −03:23:24.7 | 11.26 | 8.78 | 7.46 | ... | ... | 6.01 | 5.81 | ... |
| 14 | F | G029.2385 − 00.1911 | 18:45:22.53 | −03:22:26.4 | 8.40 | 7.09 | 6.47 | ... | ... | 6.12 | 6.07 | ... |
| 15 | C | G029.2386 − 00.1854 | 18:45:21.32 | −03:22:16.2 | 10.16 | 8.39 | 7.49 | 7.06 | ... | 6.66 | 6.69 | ... |
| 16 | C | G029.2480 − 00.2166 | 18:45:29.00 | −03:22:37.5 | 9.51 | 7.08 | 5.89 | ... | ... | 4.79 | 4.61 | ... |

**Notes.**
[a] Membership status. M denotes a member, F a foreground object, and C a cluster candidate.
[b] Ellipses indicate no listing in the GLIMPSE PSC owing to saturation.

Nine stars (numbered 1–9 in Figure 1) were chosen for spectroscopic observation based on their location (clustering) and brightness in the GLIMPSE/MIPSGAL mosaics. Table 1 lists these nine stars along with their equatorial coordinates, 2MASS *JHK* and GLIMPSE IRAC photometry. Most stars are saturated in the IRAC bands.

### 2.2. Near-IR Spectroscopy

Near-IR spectroscopy was conducted using the Mimir instrument (Clemens et al. 2007) on the Perkins 1.8 m telescope, located outside Flagstaff, Arizona, on the UT nights of 2008 May 21, June 25–28, and September 23. Mimir is a

cryogenic reimager with spectroscopic capability, delivering up to a 10 × 10 arcmin field of view to a 1024 × 1024 InSb ALADDIN III array detector at 0.6 arcsec pixel$^{-1}$. Read noise is typically 17–18 e$^-$ rms.

All spectroscopy used the *JHK*-grism (120 $l$ mm$^{-1}$, 30° blaze angle, CaF2 substrate with 29° wedge) in conjunction with one of three long-pass (LP) filters and the wide-field, F5, camera optics to yield spectra with resolutions of 430–780, for *J* band through *K* band, respectively. All May and some June observations used the 1.16 $\mu$m LP filter to yield spectra unaliased to 2.27 $\mu$m, while the remaining June observations use the 1.90 $\mu$m LP to form spectra to 2.5 $\mu$m. September observations used a 1.4 $\mu$m LP to simultaneously observe the full *H* and *K* bands.

The slit used has projected sizes of 1.2 arcsec (2 pixels) by 5 arcmin and was oriented north–south. Spectra were typically exposed for 15–45 s then moved along the spatial direction and another spectrum obtained. This A-B cycle was repeated for five or six pairs. The dome was rotated to cover the telescope beam, and exposures were taken with continuum lamps on and off in order to produce spectral flat fields. Spectral images of an argon lamp positioned over the slit were obtained for wavelength calibration. For calibration of the wavelength dependence of atmospheric transmission, spectroscopy of bright A0V stars was performed using all of the same steps, for stars chosen to be within 15 degrees and 0.1 air masses of the target stars.

Data reduction used custom IDL-based programs that included measuring and correcting the nonlinear response of the InSb photovoltaic pixels, using the fourth-order method described in Clemens et al. (2007), in addition to the usual dark and flat-field corrections. Wavelength calibration utilized the argon spectra to ascertain the two-dimensional spatial-dispersion coefficients necessary to remap the spectral images into uniformly dispersed versions. Typical dispersion solution scatter was at or under 0.1 pixels (0.14 nm) for all argon spectra. Target spectral images were flattened, interpolated, and remapped to 20 subpixels for each raw pixel, then rebinned to twice the original dispersion to achieve a fixed channel spacing and common reference wavelength.

Spectra were modeled on the images as sloped lines with "bow tie" spatially broadened extrema, due to the grism action. Spectra were extracted from the modeled locations by fitting locally sloped backgrounds at each spectral channel outside the spatial extent covered by the spectra, then integrating the signal above the background over the 2–3 rows showing significant emission. Noise was estimated for each extracted spectral channel based on Gaussian read noise and Poisson background and signal contributions. This somewhat overestimates the noise for these 2:1 synthetic channels. Relative scaling factors for each of the 10–12 spectra for a target were found across either the *H*- or *K*-band. For each spectral channel, the 10–12 scaled values were tested to remove bad pixels or cosmic rays, using median filtering. The surviving data were averaged using weighting by inverse noise squared.

Telluric spectra were developed using the A0V standard star extracted spectra and the SpeXTool program XTelcor by Cushing et al. (2004) and used to correct the target star spectra. The final spectra were flattened by identifying wavelengths free of lines, fitting baselines, and dividing by the baseline functions to yield relative intensity spectra. The resulting spectra, normalized by their error-propagated noise spectra, showed signal-to-noise ratios of 200–450.

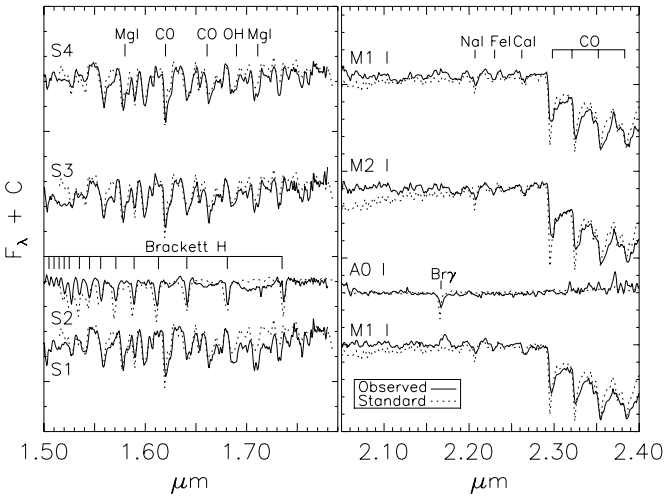


**Figure 3.** Spectra for stars S1–S4. The wavelengths cover approximate *H*- and *K*-band ranges. Our observations are the solid black lines, while smoothed atlas spectra are shown as dotted lines. The spectral types for the atlas stars are given, and the most prominent spectral features are labeled.

### 2.3. $^{13}$CO Molecular Line Data

As a means of assessing the molecular environment of the cluster, we used data cubes from the BU-FCRAO GRS[4] (Jackson et al. 2006), which mapped the $^{13}$CO $J = 1 \rightarrow 0$ molecular line in the first Galactic quadrant from $l = 18°$ to 55.°7 and $|\ b\ | \leqslant 1°$. The FCRAO 14 m telescope has a beam size of 46″ FWHM; the spectra were smoothed to a velocity resolution of 0.21 km s$^{-1}$, and cover a local standard of rest (LSR) velocity range from −5 to 135 km s$^{-1}$. The rms channel sensitivity of the GRS is 0.4 K $T_A^*$.

## 3. ANALYSIS

### 3.1. Near-IR Spectra

Near-IR spectra of the first nine potential cluster members are displayed in Figures 3 and 4. The solid lines show portions of the normalized *H*-band and *K*-band spectra for each star, shifted by arbitrary offsets for clarity. The dashed lines show *H*-band spectra from Meyer et al. (1998) and *K*-band spectra from Wallace & Hinkle (1997)[5] for the nearest available spectral type. The spectra of Meyer et al. (1998) and Wallace & Hinkle (1997) have a resolution $R = 3000$, which we smoothed by a factor of 10 to match the resolutions of our data. Eight of the nine stars (S1 and S3–S9) show deep CO band head features near 2.3 $\mu$m, characteristic of cool, evolved stars. These spectra are most consistent with late-type giants or supergiants.

Star S2, unlike the rest, is best matched with an early A or late B supergiant spectrum. This determination is based on the presence of strong Brackett series features in the *H*-band and Brackett $\gamma$ near 2.17 $\mu$m. The *H*-band Brackett lines of S2 were only about half as wide as the same lines in the A0V comparison stars, confirming its low-gravity, supergiant status. The lack of

[4] GRS data can be obtained from the Boston University Web site http://www.bu.edu/galacticring/.

[5] The data were obtained from the NOAO Digital Library http://www.lsstmail.org/dpp/library.html

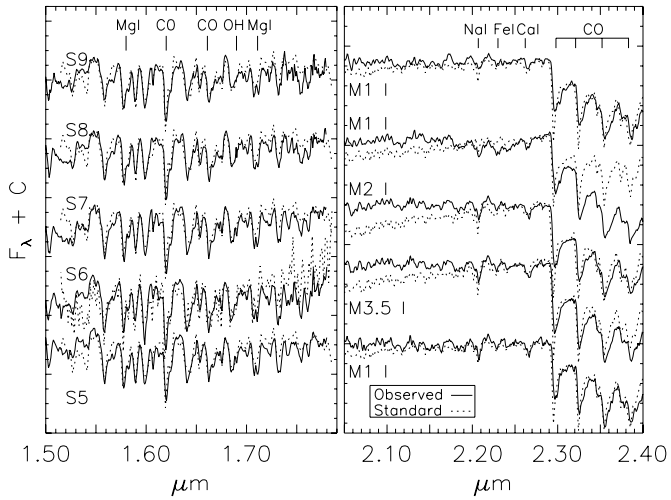


**Figure 4.** Spectra for stars S5–S9, as in Figure 3.

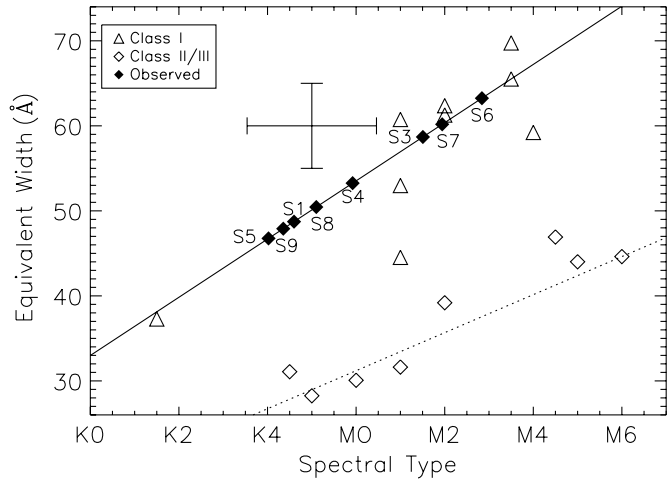


**Figure 5.** Equivalent width of the CO band head vs. spectral type. The open triangles show supergiants and open diamonds show giants from the stellar spectral atlases of Meyer et al. (1998) and Wallace & Hinkle (1997). The solid and dashed lines are least-squares fits to the supergiant and giant sequence, respectively. The filled diamonds are our sources, placed along the best-fitting line for supergiants. The cross represents our uncertainties of ±5 Å and ±2 subtypes for each star.

molecular absorption features (e.g., CO) is another indication that S2 is an early-type star.

Following the method outlined by Figer et al. (2006) (see their Figure 8), we measured the equivalent width (EW) of the first $^{12}$CO overtone feature at 2.30 $\mu$m for each star (except S2 as it shows no CO absorption). EW values were found by setting the continuum level to be the average value of the normalized flux between 2.28 and 2.30 $\mu$m and integrating the absorption between 2.30 and the pseudocontinuum longward of 2.32 $\mu$m. The same method was used for the observed stars as well as stars with known spectral types from Wallace & Hinkle (1997). Figure 5 shows the correlation between EW and spectral type for the atlas stars of supergiant (open triangles) and giant (open diamonds) luminosity classes. The solid line is a least-squares fit to 14 G3–M6 supergiants, and the dashed line is a least-squares fit to eight G7–M4 giants. This linear dependence extends all the way down to G3 spectral classes, however, we only show spectral types K0–M7 in Figure 5 for clarity. The giants

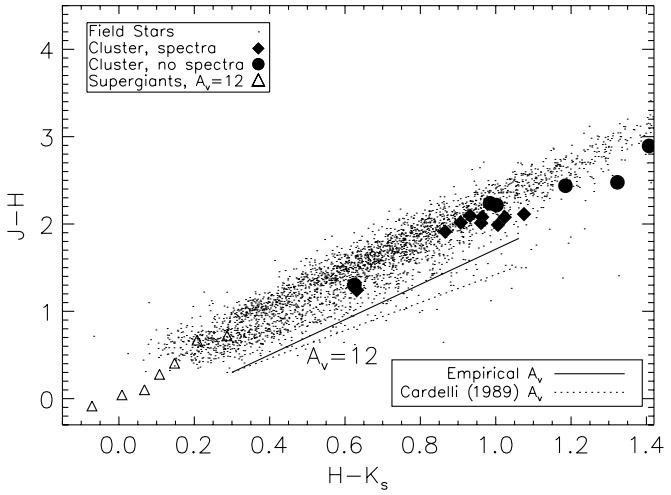


**Figure 6.** 2MASS $J - H$ vs. $H - K_s$ color–color diagram of the field in Figure 1. The small dots designate every point source in Figure 1 with accurate ($\sigma < 0.3$ mag) $JHK_s$ photometry. The filled diamonds designate the nine stars with near-IR spectra. The filled circles denote other stars near the cluster core with $K_s < 8$. The open triangles mark the fiducial unextincted supergiant sequence. The solid line shows a reddening vector for $A_V = 12$ mag.

show systematically lower EW than supergiants for a given spectral type. The strong correlation between EW and spectral type, along with the systematic differences between giants and supergiants, shows that even at relatively low spectral resolution, our IR spectra can be used to discern spectral and luminosity classes. Typical values for the EW of cluster members are 45–65 Å, which we used to assign the spectral types according to the best-fit line; these are shown as solid diamonds in Figure 5. We have estimated our uncertainty on the EW to be ±5 Å and given the slope of the least-squares fit, this corresponds to ±2 subtypes. Table 1 lists these adopted spectral types.

### 3.2. IR Photometry

Figure 6 is a 2MASS $J - H$ versus $H - K_s$ color–color diagram showing the nine stars with spectral types (filled diamonds), bright ($K_s < 8$) stars within ~4 arcmin of the cluster center (filled circles), and field stars in Figure 1 (dots). The open triangles with labels denote standard $JHK_s$ colors for supergiant stars.[6] The dotted line is the reddening vector using the Cardelli et al. (1989) extinction law, and the solid line is an empirical reddening vector based on the slope of the locus of points. This was done to attempt to correct for the deviation in the data from the Cardelli et al. (1989) reddening. The difference between the slopes corresponds to $\Delta(J - H) = 0.25$ over 12 mag of visual extinction. Since $J - H$ offset is small compared to our estimated error, we still adopt the Cardelli et al. (1989) reddening law for our data analysis. Eight of the nine stars with near-IR spectral measurements occupy a limited region of the color–color diagram—$\langle J - H \rangle \simeq 2.0$, $\langle H - K_s \rangle \simeq 1.0$—consistent with similarly reddened late-type supergiants. S2 has a much different color than the rest of the stars, suggesting an earlier spectral type. Of the other bright stars without spectral types, S14 is similar to S2 and less red than most cluster members, while S11, S13, and S16 are more red, suggesting that they may

[6] The photometric data are in the 2MASS $JHK_s$ color system, so we used transformations from Carpenter (2001) and Bessell & Brett (1988) to convert the data from Whittet & van Breda (1980), Elias et al. (1985), and Koornneef (1983) to the 2MASS filter system.

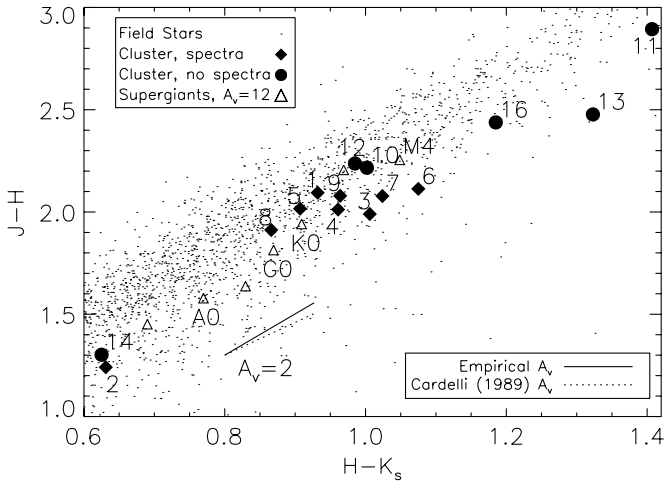


**Figure 7.** Enlarged 2MASS color–color diagram as in Figure 6, with the fiducial supergiant sequence reddened by $A_V = 12$. A reddening vector for $A_V = 2$ is shown. The reddened M-type supergiant standards match the colors of the cluster stars. S2, an A0I, is less red than expected and is probably a foreground object.

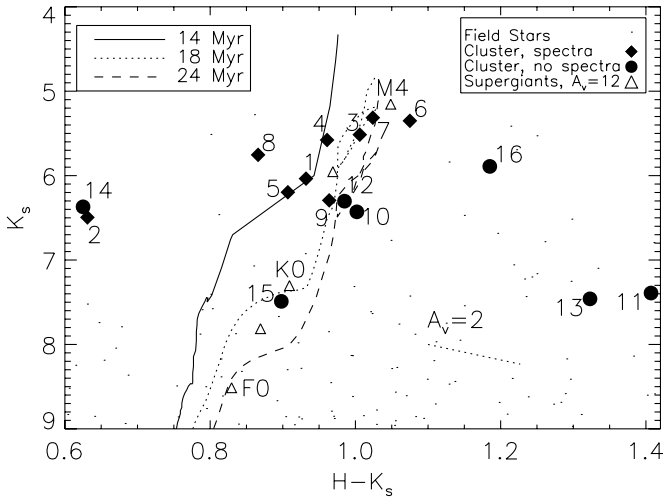


**Figure 8.** Color–magnitude diagram of stars in the field of Figure 1, with labeling as in Figure 6. Reddened (Cardelli et al. 1989) isochrones with ages of 14 Myr (solid), 18 Myr (dotted), and 24 Myr (dashed) at a distance of 7.0 kpc are shown. M-type supergiants match many of the cluster stars, while S2 is less red and more than 2.5 mag brighter than a comparable A supergiant star (off figure) at the same distance. The best-fit age is somewhere between 18 and 24 Myr. Note the presence of several stars (S10, S12, S15) with photometry but lacking spectroscopy (filled circles) that have similar colors and magnitudes as confirmed by M supergiants, suggesting the presence of several more supergiant members. S14 was shifted up by 0.1 mag for clarity.

be more heavily extincted. Stars S10 and S12 have similar colors to the majority of supergiants, suggesting that they may also be RSG cluster members. Using the reddening law of Cardelli et al. (1989), we converted the 2MASS colors, $J - K_s$ and $H - K_s$, into an average extinction. We find a mean extinction of $A_V = 12.6 \pm 0.5$ ($A_{K_s} = 1.5 \pm 0.1$).

Figure 7 is an enlarged version of Figure 6, with the fiducial supergiant colors reddened by $A_V = 12$ using the empirical relation mentioned previously. Most of the stars show colors matching K through M supergiants, with some differential extinction among cluster members. However, S2 does not match the expected A0I supergiant at $H - K_s = 0.77$ and $J - H_s = 2.1$. S2 appears to be less reddened by

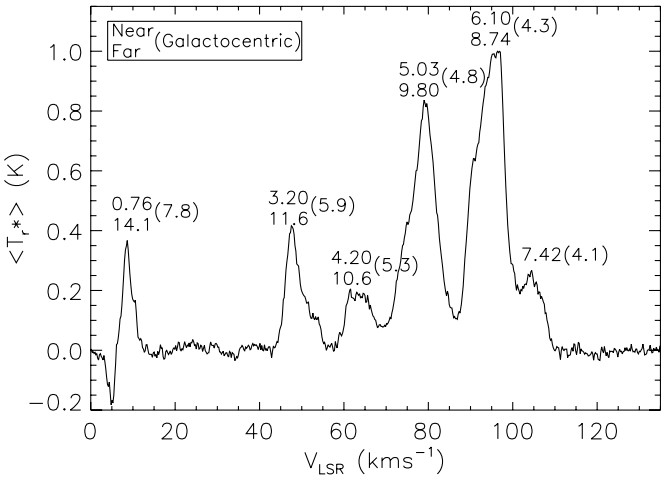


**Figure 9.** $^{13}$CO spectrum averaged over the area shown in Figure 1, showing at least five $^{13}$CO peaks along this sightline. Numbers above each peak denote the near and far heliocentric kinematic distances in kpc based on the Clemens (1985) rotation curve, while numbers in parentheses indicate the corresponding Galactocentric distance. We identify the cluster with the molecular feature near 95 km s$^{-1}$ (see the text).

1–2 mag. This indicates that S2 (and S14) are likely foreground objects.

### *3.3. Molecular Environment and a Kinematic Distance*

We used the GRS $^{13}$CO data cubes to survey the molecular environment near this RSG cluster. Figure 9 shows a plot of the $^{13}$CO brightness temperature versus LSR velocity averaged across the field of view pictured in Figure 1. This figure shows two strong $^{13}$CO peaks at LSR velocities of roughly 79 and 95 km s$^{-1}$ and several smaller peaks at 8, 47, 64, and 101 km s$^{-1}$. The abundance of $^{13}$CO components shows that this is a complex sightline with many molecular complexes at various distances. Numbers above each peak indicate the corresponding near and far heliocentric kinematic distances of $d_{\rm kin} = 5.0/9.8$ kpc and 6.1/8.7 kpc for the two major peaks and 0.7/14.1 kpc, 3.2/11.6 kpc, 4.2/10.6 kpc, and ∼7.4 kpc[7] for the lesser peaks, respectively. The numbers in parentheses above each peak indicate the Galactocentric distance for the given velocity. These distances are derived from the Galactic rotation curve of Clemens (1985), assuming $R_0 = 8.5$ kpc, $\theta_0 = 220$ km s$^{-1}$. The more recent rotation curve of Levine et al. (2008) yields very similar distances for the same $R_0$ and $\theta_0$. Adopting $R_0 = 7.6$ kpc instead (Eisenhauer et al. 2005) would reduce all distances by about 10%. We estimate the kinematic distance uncertainty at ±15% based on the width of the $^{13}$CO features.

Maps of integrated intensity were created for each of the five spectral features and compared to the GLIMPSE images. Four of the features showed no correlation between the CO and GLIMPSE images. For the fifth feature, with a peak at 95 km s$^{-1}$, a strong correlation of the CO distribution with the GLIMPSE 8 $\mu$m distribution was seen, as was a distinct anticorrelation with the location of the stellar cluster.

In Figure 10, we overlay a map of the GRS $^{13}$CO brightness temperature at 95 km s$^{-1}$, averaged between 86 and 101 km s$^{-1}$, on the GLIMPSE images. The GLIMPSE [4.5] and [8.0] bands are shown in blue and green, respectively, while the $^{13}$CO is shown in red, along with white contours. This velocity range exhibits a striking absence of molecular gas at the location of

[7] This is the unique tangent-point distance corresponding to 103 km s$^{-1}$.

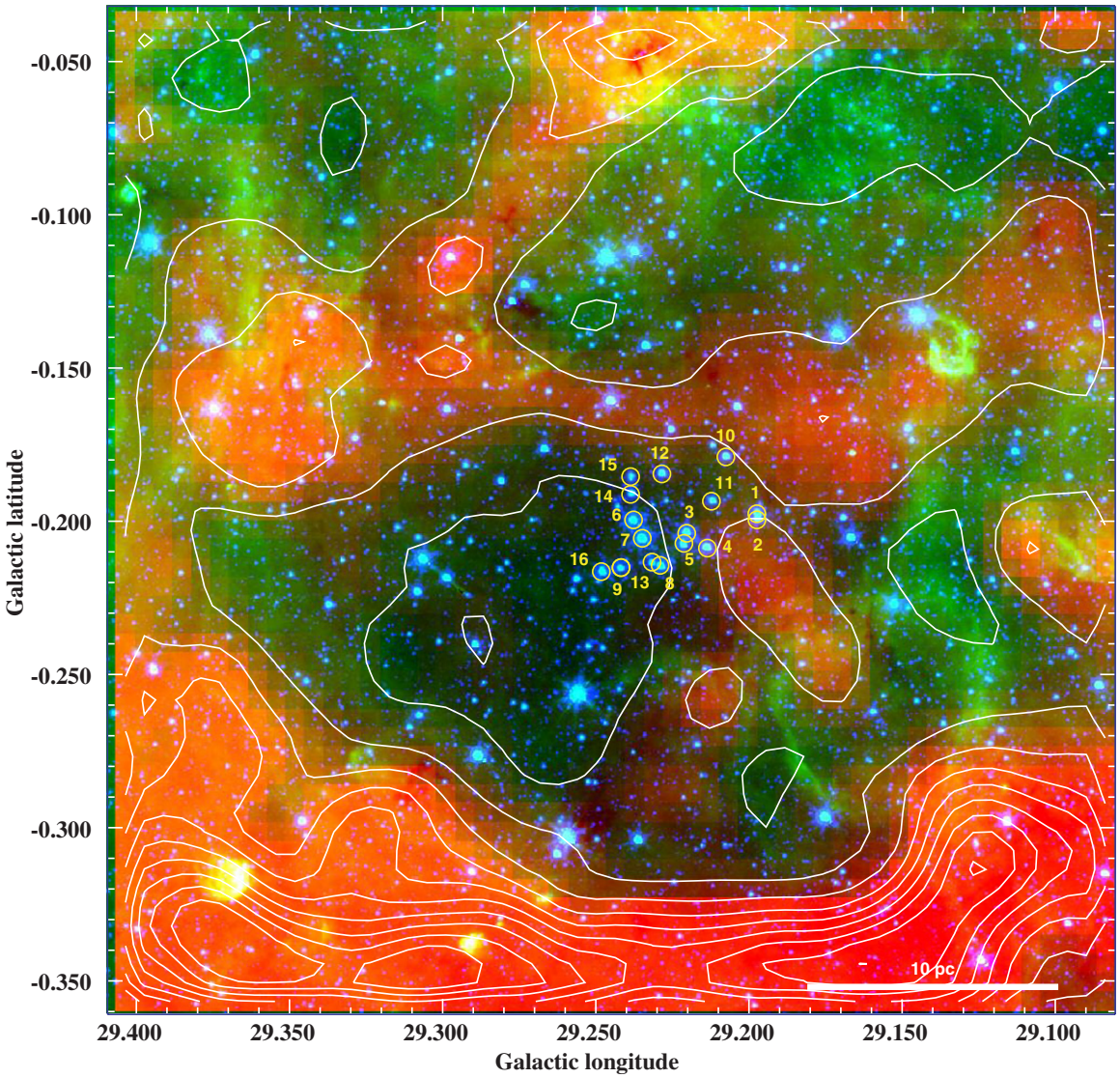


**Figure 10.** Three-color image of the cluster region with 4.5 $\mu$m in blue, 8.0 $\mu$m in green, and the GRS $^{13}$CO data averaged over the velocity range 86–101 km s$^{-1}$ ($d_{\rm kin} \simeq 6.1$ kpc/8.7 kpc) in red with $^{13}$CO contours in white. Contours range from $T_A^* = 0.1$ K to $T_A^* = 20.1$ K in increments of 2.0 K. The cluster lies near the $^{13}$CO minimum, suggestive of a cavity blown by the stellar winds of the massive cluster members.

the cluster while the surrounding regions are $^{13}$CO-bright. This $^{13}$CO minimum coincides with the 8.0 $\mu$m hole discussed earlier in connection with Figure 1. We interpret this feature to be a hole in the interstellar medium (ISM) formed by the winds of massive stars that have already evolved over the lifetime of the cluster. This velocity range, which peaks at 94 km s$^{-1}$, has a near kinematic distance of 6.1 kpc and a far kinematic distance of 8.7 kpc. Distinguishing between these two possibilities requires an independent distance measurement.

### *3.4. A Spectrophotometric Cluster Distance*

Spectroscopic parallax is commonly used to find distances when the relation between spectral type and absolute magnitude is well known and has small dispersion (e.g., for MS stars). Red supergiants, however, exhibit a large range of luminosities, spanning several magnitudes at any given spectral type. This is seen in the evolutionary tracks from Marigo et al. (2008), which are nearly vertical at the coolest temperatures. The large dispersion of absolute magnitudes among RSGs in Levesque et al. (2005) supports this empirically. In order to estimate a spectrophotometric distance for the cluster, we calculated the mean absolute $V$ magnitude and standard deviation for RSG spectral types K3–M4.5 (representative of our sample) from Levesque et al. (2005). By adopting a mean intrinsic $V - K$ color of 4.2 (Levesque et al. 2005), we derive a mean absolute $K$ magnitude for RSGs of $M_K = -10.0 \pm 0.9$. Given our mean observed $K$ magnitude of 5.75 and extinction $A_K = 1.5$ for our sample (excluding the possible foreground star S2), we estimate a distance of $7.0^{+3.7}_{-2.4}$ kpc.

Since the spectrophotometric distance is highly uncertain, we can only broadly constrain the distance of the cluster using spectroscopic parallax to the broad range 4–11 kpc, which encompasses both kinematic distances. For the purposes of determining a cluster age below, we will adopt the spectrophotometric distance of 7.0 kpc.

### *3.5. Cluster Age*

Figure 8 shows a $K_s$ versus $H - K_s$ color–magnitude diagram, along with the fiducial supergiant sequence, at a distance of

**Table 2**
Known RSG Clusters

| Name | $\ell$ (°) | b (°) | R.A.(J2000) | Decl.(J2000) | N RSGs | Age (Myr) | D (kpc) | $A_V$ (mag) | Mass ($M_\odot$) | $R_{\rm Gal}$ (kpc) |
|---|---|---|---|---|---|---|---|---|---|---|
| This cluster | 29.2 | −0.20 | 18:45:20 | −03:24:43 | 8–14 | 18–24 | 7.0 | ∼12 | ∼20,000 | 3.9 |
| RSGC1[a] | 25.2 | −0.15 | 18:37:58 | −06:52:53 | 14 | 12 ± 2 | 5.8,6.5[c] | 24 | 30,000 − 40,000 | 3.5 |
| RSGC2[b] | 26.2 | −0.06 | 18:39:20 | −06:01:41 | 26 | 17 ± 3 | 5.8 | 13 | 40,000 | 3.5 |

**Notes.**
[a] Figer et al. (2006).
[b] Davies et al. (2007).
[c] Nakashima & Deguchi (2006).

7.0 kpc and reddened by $A_V = 12$. Symbols are the same as Figure 6. The solid, dotted, and dashed curves are 14, 18, and 24 Myr isochrones[8] from Marigo et al. (2008). They have been reddened by $A_V = 12$ and placed at a distance of 7.0 kpc. The majority of the cluster stars are consistent with being reddened supergiants at 7.0 kpc for ages between 14 and 24 Myr. Note that two objects with photometry but lacking spectroscopy, S10 and S12, fall in the same region as spectroscopically confirmed RSGs, bringing the total number of probable red supergiants in the cluster to 10. Another object, S15, closely matches the G0I fiducial point. There are five other candidates, S2, S11, S13, S14, and S16 that lie very close to the center of the cluster spatially, but do not occupy the same color-magnitude space. The A0 I star, S2, is much less red and nearly 2 mag brighter than it should be if it were a cluster member. As stated previously we consider S2 to be a foreground star, not associated with the cluster. Based on the same criteria (but lacking spectroscopy) S14 is also likely to be a foreground object. Stars S11, S13, and S16 may be background objects or possibly cluster members enshrouded by additional intracluster or circumstellar dust. Massey et al. (2005) show that supergiants may be surrounded by up to 5 visual magnitudes of circumstellar extinction. Thus, we consider stars S11, S13, and S16 as candidate cluster supergiants, given their brightness and proximity to the cluster core. From Figure 8 we are then able to conclude that the cluster contains eight spectroscopically confirmed supergiants as well as six additional cluster candidates.

The most massive stars remaining in each isochrone are 18.6 $M_\odot$, 14.9 $M_\odot$, and 12.6 $M_\odot$ corresponding to ages of 14 Myr, 18 Myr, and 24 Myr. These stars are the most luminous objects in the cluster in the near-IR, so the excellent agreement between the tips isochrones and the cluster supergiants indicates that the data are consistent with an age range of 18–24 Myr. Examination of the 20 cm radio continuum map of this region from the NRAO VLA Sky Survey (Condon et al. 1998) shows no sources of emission at the location of the cluster, consistent with an older age and lack of ionizing photons from the most massive stars.

### *3.6. Cluster Stellar Mass*

The eight confirmed and 3–6 additional candidate RSGs in the cluster imply a large total stellar mass, and, given the short relative lifetime of the RSG phase, a short star formation timescale. Davies et al. (2008) compute Monte Carlo population synthesis models with a Salpeter IMF (Salpeter 1955) and Geneva isochrones (Meynet & Maeder 2000) to estimate the number of RSGs as a function of age for a range of initial cluster masses. Based on their Figure 8, a cluster containing 10 RSGs at an age of 18–24 Myr has a initial mass of ∼20,000 $M_\odot$. In this cluster, all stars except the most luminous supergiants are faint due to its distance and reddening, which means the underlying cluster is below the detection threshold for 2MASS.

## 4. DISCUSSION AND CONCLUSIONS

This newly discovered cluster resembles two other RSG clusters in terms of stellar mass, age, the high number of red supergiants, and placement in the Galaxy. Table 2 summarizes the locations and derived parameters for the clusters RSGC1 (Figer et al. 2006; Davies et al. 2008), RSGC2 ≡ Stephenson 2 (Stephenson 1990; Davies et al. 2007), and the present cluster. We have listed the distances for each cluster based on published data and computed the Galactocentric distance, $R_{\rm Gal}$, based on a solar Galactocentric distance of 7.6 kpc (Eisenhauer et al. 2005). Although the uncertainties of the spectrophotometric distances are several kiloparsecs, the resulting locations at $\ell = 25°$–$29°$ and $R_{\rm gal} = 3.5$–$3.7$ kpc indicate that these clusters may lie within a few hundred parsecs of each other. Davies et al. (2007) suggest that this is where the Scutum-Crux spiral arm meets the Galactic bulge and is within a stellar ring proposed by Bertelli et al. (1995). This location may also lie near the northern end of the Galactic bar, the parameters of which are still uncertain. There is evidence for at least two nonaxisymmetric structures in the inner Galaxy, a vertically thick triaxial bulge/bar of half-length 3.5 kpc and angle 20–35 deg (Bissantz & Gerhard 2002; Gerhard 2001; Babusiaux & Gilmore 2005) and a vertically thinner "Long Bar" of half-length 4.4 kpc and angle 40–45 deg (Hammersley et al. 2000; Benjamin et al. 2005). RSGC1, RSGC2, and this new cluster lie near the end of the Long Bar, perhaps where it meets the Scutum-Crux spiral arm and or the Molecular Ring.

Figure 11 plots the locations of RSGC1 and RSGC2 (asterisk) and the newly discovered cluster (triangle). The thick dashed lines show the spiral arms as defined by Nakanishi & Sofue (2006). The thin contours show the stellar bar as modeled by Bissantz & Gerhard (2002) from 2MASS near-IR photometry, while the thick solid curve shows the 4.4 kpc radius bar inferred by Benjamin et al. (2005) from Section ST mid-IR photometry. The location of all three RSG clusters near the end of the bar is consistent with recent star formation, possibly induced by radial gas flows along the bar. Numerical simulations show radial flows resulting from barred potentials (Schwarz 1981; Combes & Gerin 1985; Englmaier & Gerhard 1997; Piner et al. 1995; Rodriguez-Fernandez & Combes 2008). Observational studies of star formation in other galaxies also reveal enhanced activity associated with bars, sometimes along the bars themselves and

[8] Isochorones obtained from http://stev.oapd.inaf.it/cmd

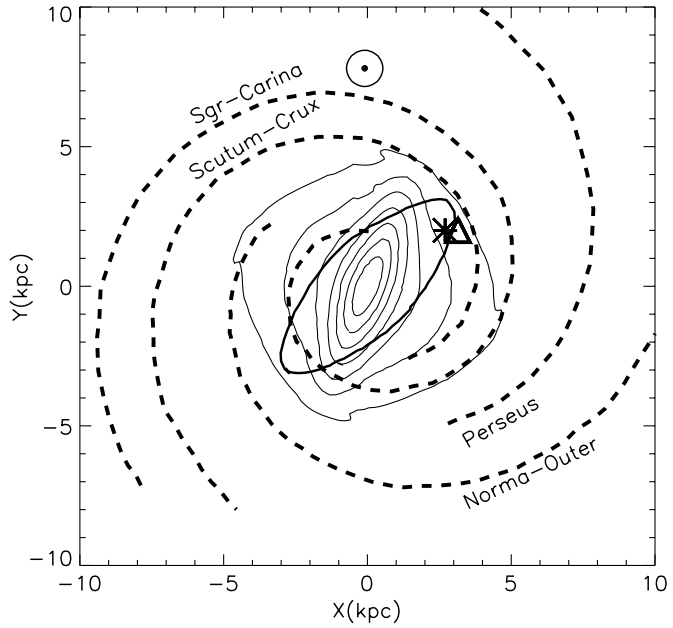


**Figure 11.** Schematic of face-on Milky Way showing the locations of RSGC1 and RSGC2 (asterisk) and the newly discovered cluster (triangle). The symbol sizes represent the uncertainties in the clusters' locations. The thick dashed curves denote spiral arms as described by Nakanishi & Sofue (2006). The thin contours show the triaxial/bulge bar as modeled by Bissantz & Gerhard (2002), while the thick solid curve shows the thin "Long Bar" as derived by Benjamin et al. (2005).

sometimes near the ends of bars where spiral arms or "spurs" attach to the bars (Martin & Friedli 1997; Sheth et al. 2002). In cases where star formation occurs along bars, it is displaced toward the leading side of the stellar bar and peaks outside of the dust and molecular lanes that run along the bar (Martin & Friedli 1997; Sheth et al. 2002). For example, Downes et al. (1996) present CO maps of the barred spiral galaxy NGC 1530 showing concentrations of molecular material near the bar ends at ∼4 kpc from the nucleus. The accompanying optical image appears to show enhanced star formation just outside this region near the bar ends. Sheth et al. (2000) report that H$\alpha$ emission peaks near the ends of the ∼4 kpc stellar bar in NGC 5383. The locations of the RSG clusters in Figure 11 near one end of the Milky Way's bar at a ∼4 kpc radius hint that a similar phenomenon may be happening in our galaxy.

Taken together, the discovery of this new cluster raises the total count of RSGs in the Galaxy and adds evidence for a localized burst of recent massive star formation. The accumulating data point toward widespread, high-mass star formation in this vicinity over the last ∼20 Myr. With a stellar mass of roughly 20,000 $M_{\odot}$ and a population containing 8–14 red supergiants, this ranks among the more massive clusters in the Galaxy.

We would like to thank Charles Kerton & Kim Arviddson for assisting with the initial discovery of this cluster and for software help. We acknowledge Bob Benjamin and Danny Dale for helpful comments. We thank an anonymous referee for a rapid and expert review. H.A.K. and M.J.A. were supported by NASA through grant NAG5-10770. This publication makes use of data products from the Two Micron All Sky Survey, which is a joint project of the University of Massachusetts and the Infrared Processing and Analysis Center/ California Institute of Technology, funded by the National Aeronautics and Space Administration and the National Science Foundation. This publication makes use of molecular line data from the Boston University Five College Radio Observatory Galactic Ring Survey (GRS), funded by the National Science Foundation under grants AST-9800334, −0098562, −0100793, −0228993, and −0507657. This research was conducted in part using the Mimir instrument, jointly developed at Boston University and Lowell Observatory and supported by NASA, NSF, and the W. M. Keck Foundation. This work was partially supported by the NSF under grant AST-0607500 to Boston University.

*Note added in proof.* As this paper went to press, we became aware of the simultaneous discovery of this star cluster by Clark et al. (2009).

## REFERENCES

Babusiaux, C., & Gilmore, G. 2005, MNRAS, 358, 1309
Benjamin, R. A., et al. 2003, PASP, 115, 953
Benjamin, R. A., et al. 2005, ApJ, 630, L149
Bertelli, G., Bressan, A., Chiosi, C., Fagotto, F., & Nasi, E. 1994, A&AS, 106, 275
Bertelli, G., Bressan, A., Chiosi, C., Ng, Y. K., & Ortolani, S. 1995, A&A, 301, 381
Bessell, M. S., & Brett, J. M. 1988, PASP, 100, 1134
Bissantz, N., & Gerhard, O. 2002, MNRAS, 330, 591
Cardelli, J. A., Clayton, G. C., & Mathis, J. S. 1989, ApJ, 345, 245
Carey, S. J., et al. 2005, BAAS, 37, 1252
Carpenter, J. M. 2001, AJ, 121, 2851
Clark, J. S., et al. 2009, arXiv:0903.1754
Clemens, D. P. 1985, ApJ, 295, 422
Clemens, D. P., Sarcia, D., Grabau, A., Tollestrup, E. V., Buie, M. W., Dunham, E., & Taylor, B. 2007, PASP, 119, 1385
Combes, F., & Gerin, M. 1985, A&A, 150, 327
Condon, J. J., Cotton, W. D., Greisen, E. W., Yin, Q. F., Perley, R. A., Taylor, G. B., & Broderick, J. J. 1998, AJ, 115, 1693
Cushing, M. C., Vacca, W. D., & Rayner, J. T. 2004, PASP, 116, 362
Davies, B., Figer, D. F., Kudritzki, R.-P., MacKenty, J., Najarro, F., & Herrero, A. 2007, ApJ, 671, 781
Davies, B., Figer, D. F., Law, C. J., Kudritzki, R.-P., Najarro, F., Herrero, A., & MacKenty, J. W. 2008, ApJ, 676, 1016
Downes, D., Reynaud, D., Solomon, P. M., & Radford, S. J. E. 1996, ApJ, 461, 186
Eisenhauer, F., et al. 2005, ApJ, 628, 246
Elias, J. H., Frogel, J. A., & Humphreys, R. M. 1985, ApJS, 57, 91
Englmaier, P., & Gerhard, O. 1997, MNRAS, 287, 57
Fazio, G. G., et al. 2004, ApJS, 154, 10
Figer, D. F., MacKenty, J. W., Robberto, M., Smith, K., Najarro, F., Kudritzki, R. P., & Herrero, A. 2006, ApJ, 643, 1166
Gerhard, O. E. 2001, in ASP Conf. Ser. 230, Galaxy Disks and Disk Galaxies, ed. J. G. Funes, S.J., & E. M. Corsini, (San Francisco, CA: ASP), 21
Hammersley, P. L., Garzón, F., Mahoney, T. J., López-Corredoira, M., & Torres, M. A. P. 2000, MNRAS, 317, L45
Jackson, J. M., et al. 2006, ApJS, 163, 145
Kobulnicky, H. A., et al. 2005, AJ, 129, 239
Koornneef, J. 1983, A&A, 128, 84
Levesque, E. M., Massey, P., Olsen, K. A. G., Plez, B., Josselin, E., Maeder, A., & Meynet, G. 2005, ApJ, 628, 973
Levine, E. S., Heiles, C., & Blitz, L. 2008, ApJ, 679, 1288
Marigo, P., Girardi, L., Bressan, A., Groenewegen, M. A. T., Silva, L., & Granato, G. L. 2008, A&A, 482, 883
Martin, P., & Friedli, D. 1997, A&A, 326, 449
Massey, P., Plez, B., Levesque, E. M., Olsen, K. A. G., Clayton, G. C., & Josselin, E. 2005, ApJ, 634, 1286
Mercer, E. P., et al. 2005, ApJ, 635, 560
Meyer, M. R., Edwards, S., Hinkle, K. H., & Strom, S. E. 1998, ApJ, 508, 397
Meynet, G., & Maeder, A. 2000, A&A, 361, 101
Nakanishi, H., & Sofue, Y. 2006, PASJ, 58, 847
Nakashima, J. I., & Deguchi, S. 2006, ApJ, 647, L139
Piner, B. G., Stone, J. M., & Teuben, P. J. 1995, ApJ, 449, 508

Rieke, G. H., et al. 2004, ApJS, 154, 25
Rodriguez-Fernandez, N. J., & Combes, F. 2008, A&A, 489, 115
Salpeter, E. E. 1955, ApJ, 121, 161
Schwarz, M. P. 1981, ApJ, 247, 77
Sheth, K., Regan, M. W., Vogel, S. N., & Teuben, P. J. 2000, ApJ, 532, 221
Sheth, K., Vogel, S. N., Regan, M. W., Teuben, P. J., Harris, A. I., & Thornley, M. D. 2002, AJ, 124, 2581
Skrutskie, M. F., et al. 2006, AJ, 131, 1163
Stephenson, C. B. 1990, AJ, 99, 1867
Wallace, L., & Hinkle, K. 1997, ApJS, 111, 445
Whittet, D. C. B., & van Breda, I. G. 1980, MNRAS, 192, 467